
Measurement Embedded Schrödinger Bridge for Inverse Problems

Yuang Wang

Department of Engineering Physics, Tsinghua University, Beijing, China
Department of Radiology, Massachusetts General Hospital and Harvard Medical School, Boston, USA

Pengfei Jin

Department of Radiology, Massachusetts General Hospital and Harvard Medical School, Boston, USA

Siyeop Yoon

Department of Radiology, Massachusetts General Hospital and Harvard Medical School, Boston, USA

Matthew Tivnan

Department of Radiology, Massachusetts General Hospital and Harvard Medical School, Boston, USA

Quanzheng Li

Department of Radiology, Massachusetts General Hospital and Harvard Medical School, Boston, USA

Li Zhang

Department of Engineering Physics, Tsinghua University, Beijing, China

Dufan Wu*

Department of Radiology, Massachusetts General Hospital and Harvard Medical School, Boston, USA

Abstract

Score-based diffusion models are frequently employed as structural priors in inverse problems. However, their iterative denoising process, initiated from Gaussian noise, often results in slow inference speeds. The Image-to-Image Schrödinger Bridge (I^2SB), which begins with the corrupted image, presents a promising alternative as a prior for addressing inverse problems. In this work, we introduce the Measurement Embedded Schrödinger Bridge (MESB). MESB establishes Schrödinger Bridges between the distribution of corrupted images and the distribution of clean images given observed measurements. Based on optimal transport theory, we derive the forward and backward processes of MESB. Through validation on diverse inverse problems, our proposed approach exhibits superior performance compared to existing Schrödinger Bridge-based inverse problems solvers in both visual quality and quantitative metrics.

1 Introduction

Inverse problems are prevalent across various scientific and engineering disciplines with the aim of uncovering an unknown signal from observed measurements. The inherent complexity arises from

*Corresponding author: dwu6@mgh.harvard.edu

their ill-posed nature, where multiple solutions can plausibly explain the observed data. To address this challenge, score-based diffusion models [1; 2; 3] are commonly employed as a structural prior, facilitating the derivation of meaningful solutions. Numerous techniques have been developed to integrate data consistency into the sampling process of diffusion models and maintain the sample path on the data manifold[4; 5; 6; 7]. While diffusion-based inverse problem solvers have achieved success in image restoration tasks, their inference speed is often hampered by the need for a large number of iterative denoising steps to generate clean images from pure Gaussian noise.

Instead of starting from Gaussian noise, Schrödinger Bridges[8; 9; 10; 11; 12] establish diffusion bridges between the distributions of clean and corrupted images. By initializing the diffusion process with the corrupted image, which is closer to the clean one compared to Gaussian noise, Schrödinger Bridges offer a promising approach for generating high-quality conditional samples with fewer diffusion steps. One notable example is the Image-to-Image Schrödinger Bridge (I²SB)[13], which models the diffusion bridge between paired clean and corrupted samples. This model enables efficient training by connecting it with the standard score-based diffusion model. Recently, the data Consistent Direct Diffusion Bridge (CDDB)[14] has further enhanced the performance of I²SB in both perceptual ability and fidelity to ground truth by incorporating data consistency techniques similar to those used in diffusion models.

In our research, we propose the Measurement Embedded Schrödinger Bridge (MESB) for solving inverse problems. Unlike CDDB that constructs Schrödinger Bridges between clean and corrupted image distributions and incorporates data consistency during sampling, MESB directly establishes Schrödinger Bridges between the distribution of corrupted images and the distribution of clean images given observed measurements. Based on optimal transport theory, we derive the forward and backward processes of MESB, inherently incorporating data consistency into the backward process. Our method is validated across diverse inverse problems, demonstrating superior performance compared to existing Schrödinger Bridge-based inverse problem solvers.

2 Preliminaries

Notation: Consider a d-dimensional stochastic process denoted by $X_t \in \mathbb{R}^d$, where $t \in [0, 1]$ indexes the process. We use X_{clean} to represent a sample from the clean image distribution q_{clean} and $X_{corrupt}$ for a sample from the corrupted image distribution $q_{corrupt}$. Let N be the number of generative steps. We define discrete generative time steps as $0 = t_0 < t_1 < \dots < t_n < \dots < t_N = 1$, and use the shorthand $X_n \equiv X_{t_n}$.

2.1 Schrödinger Bridge

The Schrödinger Bridge is an entropy-regularized optimal transport approach[15] that constructs diffusion bridges between two arbitrary distributions p_A and p_B . It is defined by the following forward and backward stochastic differential equations (SDEs):

$$dX_t = [f_t + \beta_t \nabla_{X_t} \log \Psi(X_t, t)] dt + \sqrt{\beta_t} dw_t, \quad (1)$$

$$dX_t = [f_t - \beta_t \nabla_{X_t} \log \hat{\Psi}(X_t, t)] dt + \sqrt{\beta_t} d\bar{w}_t. \quad (2)$$

In these equations, X_0 is sampled from p_A , X_1 is sampled from p_B , f_t represents the basic drift of X_t , β_t determines the diffusion speed, and w_t and \bar{w}_t are the Wiener process and its reversed counterpart. To ensure that the path measure induced by the forward SDE (1) is almost surely equal to the one induced by the reverse SDE (2), the time-varying energy potentials Ψ and $\hat{\Psi}$ must satisfy the following coupled partial differential equations (PDEs):

$$\begin{cases} \frac{\partial \Psi}{\partial t} = -\nabla \Psi^T f - \frac{1}{2} \beta \Delta \Psi, \\ \frac{\partial \hat{\Psi}}{\partial t} = -\nabla \cdot (\hat{\Psi} f) + \frac{1}{2} \beta \Delta \hat{\Psi}, \end{cases} \quad (3)$$

subject to the margin conditions:

$$\Psi(X_0, 0) \hat{\Psi}(X_0, 0) = p_A(X_0), \Psi(X_1, 1) \hat{\Psi}(X_1, 1) = p_B(X_1). \quad (4)$$

2.2 Score-based Diffusion Models

Score-based diffusion models[2], as a special case of the Schrödinger Bridge, specify p_A as q_{clean} and p_B as the Gaussian distribution $\mathcal{N}(0, I)$, using a linear f_t with respect to \hat{X}_t . In this setup, Ψ simplifies to 1, and $\nabla \log \hat{\Psi}$ becomes the score function and can be learned through denoising score matching[16].

2.3 Image-to-Image Schrödinger Bridge

The coupling of Ψ and $\hat{\Psi}$ in the margin conditions (4) can lead to computational challenges when setting p_A as q_{clean} and p_B as $q_{corrupt}$. I²SB[13] offers an approach to decouple Ψ and $\hat{\Psi}$. Instead of treating the clean image distribution as a continuous manifold, it is represented as a sum of delta functions centered at each clean image. By setting $p_A(X_0)$ as $\delta(X_0 - X_{clean})$, Ψ and $\hat{\Psi}$ become decoupled, enabling the establishment of a Schrödinger Bridge for each clean and corrupted image pair. With f set to 0, I²SB can be trained as efficiently as score-based diffusion models.

Specifically, in the forward process, X_t is sampled from the distribution $q(X_t|X_0, X_1)$:

$$q(X_t|X_0, X_1) = \mathcal{N}\left(X_t; \frac{\bar{\sigma}_t^2}{\bar{\sigma}_t^2 + \sigma_t^2} X_0 + \frac{\sigma_t^2}{\bar{\sigma}_t^2 + \sigma_t^2} X_1, \frac{\sigma_t^2 \bar{\sigma}_t^2}{\bar{\sigma}_t^2 + \sigma_t^2} I\right), \quad (5)$$

where $\sigma_t^2 = \int_0^t \beta_\tau d\tau$ and $\bar{\sigma}_t^2 = \int_t^1 \beta_\tau d\tau$ represent variances accumulated from either side. The network ϵ_θ can be efficiently trained to predict the difference between X_t and X_0 by minimizing the loss function:

$$\theta^* = \arg \min_{\theta} E_{X_0, X_1} E_{t \sim \mathcal{U}[0,1], X_t \sim q(X_t|X_0, X_1)} \|\epsilon_\theta(X_t, t) - \frac{X_t - X_0}{\sigma_t}\|. \quad (6)$$

In the reverse process, I²SB sets X_N as the corrupted image $X_{corrupt}$ and iteratively approaches X_0 . In the step from X_n to X_{n-1} , \hat{X}_0 , the expected mean of X_0 , is first calculated using the trained network ϵ_{θ^*} and X_n :

$$\hat{X}_0 = X_n - \sigma_n \epsilon_{\theta^*}(X_n, t_n, y), \quad (7)$$

where $\sigma_n \equiv \sigma_{t_n}$. Subsequently, X_{n-1} is sampled from the DDPM posterior $p(X_{n-1}|\hat{X}_0, X_n)$, expressed as:

$$p(X_{n-1}|X_0, X_n) = \mathcal{N}\left(X_{n-1}; \frac{\alpha_{n-1}^2}{\alpha_{n-1}^2 + \sigma_{n-1}^2} X_0 + \frac{\sigma_{n-1}^2}{\alpha_{n-1}^2 + \sigma_{n-1}^2} X_n, \frac{\sigma_{n-1}^2 \alpha_{n-1}^2}{\alpha_{n-1}^2 + \sigma_{n-1}^2} I\right), \quad (8)$$

where $\alpha_{n-1}^2 = \int_{t_{n-1}}^{t_n} \beta_\tau d\tau$ denotes the accumulated variance between consecutive time steps t_{n-1} and t_n .

3 Method

In this section, we propose MESB for inverse problems, establishing Schrödinger Bridges between the distribution of corrupted images and the distribution of clean images given measurements. We embed measurements into the margin conditions 4, obtain Ψ and $\hat{\Psi}$ by solving the PDEs (3) and (4), and derive the forward and backward processes of MESB using SDEs (1) and (2). All proofs are provided in Appendix A.1.

3.1 Measurement Embedded Schrödinger Bridge for Inverse Problems

In the context of inverse problems, we start with $X_{corrupt}$ and seek to recover X_{clean} based on the measurement y , which is related through the system matrix A and detector noise n , as described by the equation:

$$y = AX_{clean} + n. \quad (9)$$

To address this challenge, we propose MESB to establish Schrödinger Bridges that map each corrupted image to its corresponding clean image distribution given the measurement y . This is achieved by setting p_A and p_B as follows:

$$p_A(X_0) = q_{clean}(X_0|X_{corrupt}, y), \quad (10)$$

$$p_B(X_1) = \delta(X_1 - X_{corrupt}), \quad (11)$$

where $q_{clean}(\cdot|X_{corrupt}, y)$ represents the clean image distribution given specific $X_{corrupt}$ and y .

Theorem 1 *If p_A and p_B are defined according to equations (10) and (11), and f is set to 0, then the PDEs (3) and (4) have the following analytical solutions:*

$$\Psi(X_t, t) = \mathcal{N}(X_t|X_{corrupt}, \bar{\sigma}_t^2 I), \quad (12)$$

$$\hat{\Psi}(X_t, t) = \int \hat{\Psi}_{X_0}(X_t, t) q_{clean}(X_0|X_{corrupt}, y) dX_0, \quad (13)$$

where

$$\hat{\Psi}_{X_0}(X_t, t) = C_{X_0} \mathcal{N}(X_t|X_0, \sigma_t^2 I), \quad (14)$$

and

$$C_{X_0} = \left(\sqrt{2\pi}\sigma_1\right)^d \exp\left(\frac{(X_0 - X_{corrupt})^\top (X_0 - X_{corrupt})}{2\sigma_1^2}\right). \quad (15)$$

We set f to 0, and based on Theorem 1, Ψ and $\hat{\Psi}$ can be analytically expressed as equations (12) and (13). The gradient of $\log \Psi$ can be computed as:

$$\nabla \log \Psi = -\frac{1}{\bar{\sigma}_t^2} (X_t - X_{corrupt}). \quad (16)$$

By incorporating equation (16) into the forward SDE (1), we derive the forward process of MESB, which is same to that of I²SB.

For the reverse process of MESB, we need to parameterize $q_{clean}(X_0|X_{corrupt}, y)$. This conditional probability is influenced not only by the distance between X_0 and the plane $AX = y$ according to equation (9), but also by the distance between X_0 and $Z(X_{corrupt}, y)$, where Z represents a function that can approximately map $X_{corrupt}$ and y to their corresponding clean image. Thus, we assume that $q_{clean}(X_0|X_{corrupt}, y)$ can be represented as:

$$q_{clean}(X_0|X_{corrupt}, y) = k \mathcal{N}(X_0|Z(X_{corrupt}, y), \Sigma_X) \mathcal{N}(y|AX_0, \sigma_y^2 I). \quad (17)$$

Here, k is a constant independent of X_0 and X_t . The covariance matrices Σ_X and $\sigma_y^2 I$ reflect the confidence level in the approximate mapping Z and the accuracy of the measurement y , respectively. Under this assumption, we can compute the gradient of $\log \hat{\Psi}$ as:

$$\nabla \log \hat{\Psi} = -\frac{1}{\sigma_t^2} (X_t - \hat{X}_{0,new}). \quad (18)$$

In this equation, $\hat{X}_{0,new}$ is the solution of the linear equation:

$$M_t \hat{X}_{0,new} = \left(\left(X_t - \frac{\sigma_t^2}{\sigma_1^2} X_{corrupt} \right) + \sigma_t^2 \Sigma_X^{-1} Z(X_{corrupt}, y) + \frac{\sigma_t^2}{\sigma_y^2} A^\top y \right), \quad (19)$$

where M_t is defined as:

$$M_t = \left(\left(1 - \frac{\sigma_t^2}{\sigma_1^2} \right) I + \sigma_t^2 \Sigma_X^{-1} + \frac{\sigma_t^2}{\sigma_y^2} A^\top A \right). \quad (20)$$

By integrating equation (18) into the backward SDE (2), we derive the reverse process of MESB. Specifically, transitioning from X_n to X_{n-1} involves computing \hat{X}_0 using equation (7), and then solving the linear equation:

$$M_{t_n} \hat{X}_{0,new} = \left(\left(X_n - \frac{\sigma_n^2}{\sigma_N^2} X_{corrupt} \right) + \sigma_n^2 \Sigma_X^{-1} \hat{X}_0 + \frac{\sigma_n^2}{\sigma_y^2} A^\top y \right), \quad (21)$$

where we substitute the approximate mapping Z in equation (19) with \hat{X}_0 . Subsequently, X_{n-1} is sampled from $p(X_{n-1}|\hat{X}_{0,new}, X_n)$ according to equation (8). In practice, obtaining the exact solution of the linear equation (21) is time-consuming; hence, we perform a p -th Conjugate Gradient (CG) update starting from \hat{X}_0 . The generative process of MESB is summarized in Algorithm (1).

Algorithm 1 Generative Process of MESB

Input: $N, \{t_n\}, X_{corrupt}$, measurement y , system matrix A , trained network ϵ_{θ^*}

Initialize: $\hat{X}_N = X_{corrupt}$

for $n = N$ to 1 **do**

 Predict \hat{X}_0 using X_n and $\epsilon_{\theta^*}(X_n, t_n)$ according to equation (7)

 Start from \hat{X}_0 and perform p -th CG update for linear equation (21) to get $\hat{X}_{0,new}$

 Sample X_{n-1} from $p(X_{n-1}|\hat{X}_{0,new}, X_n)$ according to equation (8)

end for

return X_0

3.2 Understanding of Measurement Embedded Schrödinger Bridge

3.2.1 Simplification

For a clearer understanding of MESB, we delve into equation (21), which incorporates data consistency into the generative process. This equation can be viewed as an optimization problem:

$$\hat{X}_{0,new} = \arg \min_X \|X - \hat{X}_0\|_2^2 + k_y \|AX - y\|_2^2 + k_e \|X - X_{0,e}\|_2^2 + \|T(X - \hat{X}_0)\|_2^2, \quad (22)$$

where

$$X_{0,e} = \frac{\sigma_N^2}{\sigma_n^2} X_n - \frac{\sigma_n^2}{\sigma_n^2} X_{corrupt}, \quad (23)$$

$$k_e = \frac{\bar{\sigma}_n^2 \sigma_X^2}{\sigma_n^2 \sigma_N^2}, \quad (24)$$

and

$$k_y = \frac{\sigma_X^2}{\sigma_y^2}. \quad (25)$$

In these equations, σ_X^2 represents the largest eigenvalue of Σ_X , and T denotes a transformation matrix associated with Σ_X as described by the equation:

$$\Sigma_X^{-1} = \frac{1}{\sigma_x^2} (I + T^T T). \quad (26)$$

According to equation (22), MESB considers four essential terms in the generative process. The first term $\|X - \hat{X}_0\|_2^2$ aims to keep $\hat{X}_{0,new}$ close to \hat{X}_0 and acts as a regularization term, particularly effective when dealing with noisy measurements. The second term $\|AX - y\|_2^2$ enforces hard data consistency within $\hat{X}_{0,new}$. The third term $\|X - X_{0,e}\|_2^2$ uses information from the extrapolation term $X_{0,e}$, which might capture additional details beyond the expected mean \hat{X}_0 . Lastly, the fourth term $\|T(X - \hat{X}_0)\|_2^2$ ensures that $\hat{X}_{0,new}$ aligns with \hat{X}_0 under the transformation T , enabling the integration of prior knowledge about the clean image distribution into MESB through the design of the transformation matrix T .

3.2.2 Relationship with CDDB and CDDB deep

CDDB and CDDB-deep[14] are Schrödinger Bridge-based inverse problem solvers that use the same trained model as I²SB and incorporate data consistency during sampling, similar to the techniques used in Decomposed Diffusion Sampling (DDS)[4] and Diffusion Posterior Sampling (DPS)[5]. Specifically, in each reverse step from X_n to X_{n-1} , CDDB updates the expected mean \hat{X}_0 by:

$$\hat{X}_{0,new}^{CDDB} = \hat{X}_0 + \alpha A^T (y - A\hat{X}_0), \quad (27)$$

and CDDB-deep updates it by:

$$\hat{X}_{0,new}^{deep} = \hat{X}_0 - \alpha \nabla_{X_n} \|A\hat{X}_0(X_n) - y\|_2^2, \quad (28)$$

where the step lengths α are treated as hyperparameters. These updated means, $\hat{X}_{0,new}^{CDDB}$ and $\hat{X}_{0,new}^{deep}$, are then used for sampling X_{n-1} according to equation (8). Here, we establish the connections between our proposed MESB and CDDB as well as CDDB-deep.

Table 1: Quantitative results of tested methods for the deblur-gauss (no noise) task. **Bold**: best, under: second best.

N	LPIPS (Corrupt: 0.4291)				SSIM (Corrupt: 0.5995)			
	10	20	50	100	10	20	50	100
I ² SB	0.0620	0.0617	0.0622	0.0625	0.9490	0.9475	0.9463	0.9458
Project	<u>0.0454</u>	<u>0.0437</u>	<u>0.0424</u>	<u>0.0417</u>	<u>0.9689</u>	<u>0.9702</u>	<u>0.9714</u>	<u>0.9722</u>
CDDB	0.0538	0.0525	0.0523	0.0523	0.9593	0.9595	0.9594	0.9594
CDDB deep	0.0611	0.0601	0.0605	0.0629	0.9498	0.9491	0.9486	0.9477
Proposed	0.0440	0.0414	0.0398	0.0390	0.9716	0.9737	0.9748	0.9754

Theorem 2 *If the system matrix A satisfies the following two conditions: firstly, there exists a positive number α_0 such that $\sqrt{\alpha_0}A$ is a partially isometric matrix[17], and secondly, A is row full rank, then the CDDB update for \hat{X}_0 in equation (27) is equivalent to solving the optimization problem:*

$$\hat{X}_{0,new}^{eq} = \arg \min_X \|X - \hat{X}_0\|_2^2 + k\|AX - y\|_2^2. \quad (29)$$

Specifically, when $\alpha = \frac{\alpha_0 k}{\alpha_0 + k}$, $\hat{X}_{0,new}^{CDDB} = \hat{X}_{0,new}^{eq}$.

In applications such as pool super-resolution, inpainting, and MRI acceleration, where the system matrix A strictly satisfies the conditions described in Theorem 2, CDDB can be considered as a special case of our proposed MESB. This is because the update for \hat{X}_0 in MESB becomes equivalent to the CDDB update when setting k_e and T in equation (22) to 0. In other applications, such as deblurring and sparse-view CT reconstruction, where the system matrix A does not satisfy these conditions, a single-step gradient update cannot fully incorporate all the information from the measurements into \hat{X}_0 . In such cases, our proposed MESB, which uses hard data consistency along with regularization terms, can achieve better performance than CDDB.

Theorem 3 *If p_A and p_B are defined according to equations (10) and (11), f is set to 0, Ψ and $\hat{\Psi}$ are expressed in equations (12) and (13), and X_t is sampled from equation (5), assuming that given X_t and $X_{corrupt}$, the measurement y follows a gaussian distribution centered at $A\hat{X}_0(X_t)$:*

$$q(y|X_t, X_{corrupt}) = \mathcal{N}\left(y|A\hat{X}_0(X_t), \sigma^2 I\right), \quad (30)$$

where $\hat{X}_0(X_t)$ is the expected mean, then the gradient of $\log \hat{\Psi}$ can be expressed as:

$$\nabla \log \hat{\Psi} = -\frac{1}{\sigma_t^2} \left(X_t - \hat{X}_{0,new}^{deep}\right), \quad (31)$$

where $\hat{X}_{0,new}^{deep}$ is expressed in equation (28), and the step length α equals to $\frac{\sigma_t^2}{2\sigma^2}$.

As indicated by Theorem 3, CDDB deep can also be considered as establishing Schrödinger Bridges between p_A and p_B as defined in the equations (10) and (11), but with a different assumption to decouple $\hat{\Psi}$ and $q_{clean}(X_0|X_{corrupt}, y)$ in the equation (13). The incorporation of the U-net Jacobian in CDDB deep makes it suitable for tasks like inpainting, where a global impact on all pixels is desired. However, this incorporation also makes it more time- and memory-consuming than our proposed MESB.

3.3 Implementation Details

We validated our proposed method on both natural and medical image tasks. For natural image tasks, we used the pretrained model of I²SB[13] and evaluated our proposed MESB with 5,000 images randomly selected from the validation dataset of ImageNet 256x256[18]. We tested MESB on the following degradation tasks: gaussian deblurring with no added noise and 4x super-resolution with bicubic interpolation and 1% gaussian noise.

For the medical image tasks, we validated our proposed MESB with CT sparse view reconstruction. We used the RPLHR-CT-tiny dataset[19], consisting of anonymized chest CT volumes. The original

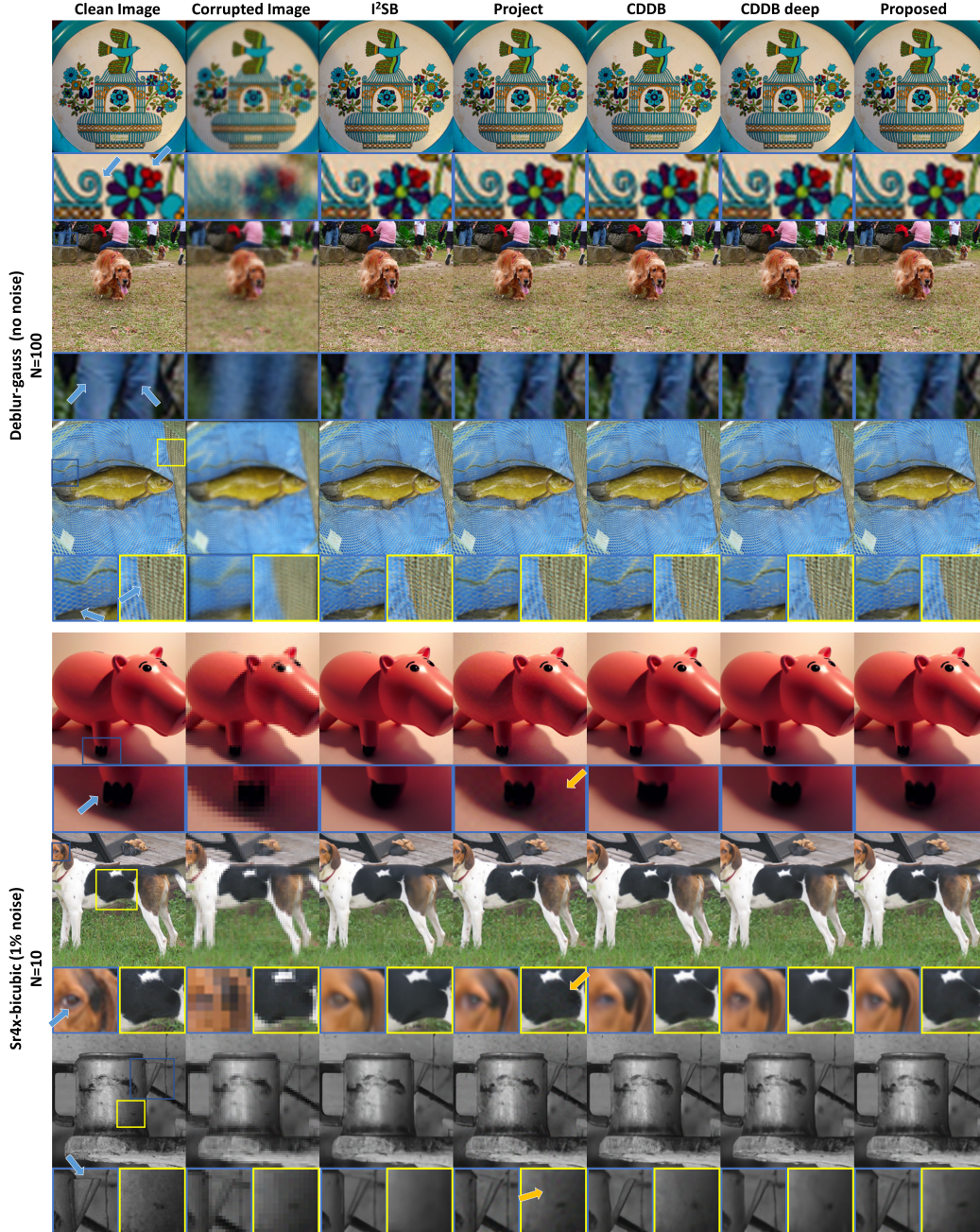


Figure 1: Visualization results for the deblur-gauss (no noise) task and the sr4x-bicubic (1% noise) task. The details within the blue and yellow boxes are zoomed in for enhanced visual clarity.

CT images served as ground truth, and the corresponding corrupted images were obtained using the FBP algorithm with projections from 60 distinct views in a fan beam geometry. We used 40 cases (11,090 slices) with 0.01% Gaussian noise added in the projections for training and 5 cases (1,425 slices) with 0.1% Gaussian noise added in the projections for testing. The neural network $\epsilon_\theta(X_n, t_n)$ we used is a 2D residual U-Net with the same architecture used in DDPM[2]. We concatenated positional encoded $X_{corrupt}$ with X_n along the channel dimension to serve as additional conditions for the network. During training, we used 1000 diffusion time steps with quadratic discretization, and adopted a symmetric scheduling[10; 12] of β_t with a maximum value of 0.15 at $t = 0.5$. The

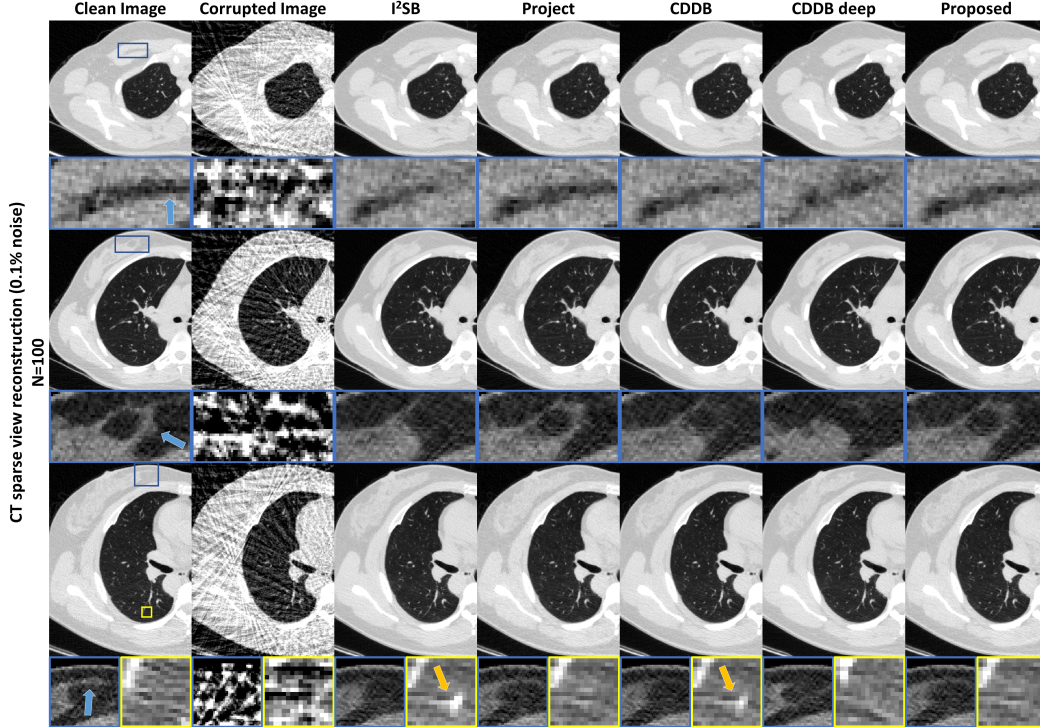


Figure 2: Visualization results for the CT sparse view reconstruction (0.1% noise) task. The details within the blue and yellow boxes are zoomed in for enhanced visual clarity. The display window for the entire images is set to [-1000HU, 200HU], for the zoomed regions outside the lungs is set to [-160HU, 200HU], and for the zoomed regions inside the lungs is set to [-1000HU, -550HU].

Table 2: Quantitative results of tested methods for the sr4x-bicubic (1% noise) task. **Bold**: best, under: second best.

N	LPIPS (Corrupt: 0.4693)				SSIM (Corrupt: 0.6633)			
	10	20	50	100	10	20	50	100
I ² SB	0.2772	0.2698	0.2633	0.2611	0.7490	0.7320	0.7111	0.6987
Project	0.2433	0.2348	0.2302	0.2314	0.7789	0.7643	0.7432	0.7289
CDDB	<u>0.2409</u>	<u>0.2294</u>	0.2197	<u>0.2171</u>	<u>0.7793</u>	0.7674	0.7505	0.7395
CDDB deep	0.2529	0.2329	0.2105	0.2082	0.7755	0.7712	0.7613	0.7452
Proposed	0.2361	0.2258	<u>0.2186</u>	0.2182	0.7829	<u>0.7703</u>	<u>0.7521</u>	0.7400

model was trained on randomly cropped patches of size 128×128 and tested on the entire 512×512 images. A batch size of 64 was employed during training, using the Adam algorithm with a learning rate of 8×10^{-5} for 200,000 iterations. The number of generative steps N was set to 10, 20, 50, and 100, and the time of CG iterations p for each reverse step was set to 5.

We specify the corrupted image $X_{corrupt}$ and the measurement y for each task. In the deblur-gauss (no noise) task, y and $X_{corrupt}$ are both blurred images. In the sr4x-bicubic (1% noise) task, y is the downsampled image, and $X_{corrupt}$ is the reconstructed image from y using nearest neighbor interpolation. In the CT sparse view (0.1% noise) task, y represents the projections and $X_{corrupt}$ is the reconstructed image from y using FBP algorithm.

The hyperparameters k_e and k_y and the transformation matrix T are set as follows. In the deblur-gauss (no noise) task, k_y is set to positive infinity, k_e is set to $20 \frac{\sigma_y^2 \sigma_x^2}{\sigma_N^4}$, and T is set to 0. In the sr4x-bicubic (1% noise) task, k_y is set to 32, k_e is set to 0, and T is set to 0. In the CT sparse view reconstruction

Table 3: Quantitative results of tested methods for CT sparse view reconstruction (0.1% noise) task. **Bold:** best, under: second best

N	LPIPS (Corrupt: 0.5034)				SSIM (Corrupt: 0.3193)			
	10	20	50	100	10	20	50	100
I ² SB	0.2236	0.2082	0.1910	0.1838	0.9192	0.9141	0.9055	0.8981
Project	<u>0.2199</u>	0.2087	0.1975	0.1938	<u>0.9208</u>	<u>0.9171</u>	<u>0.9104</u>	<u>0.9041</u>
CDDB	0.2219	<u>0.2065</u>	<u>0.1893</u>	0.1815	0.9203	0.9160	0.9075	0.9020
CDDB deep	0.2226	0.2072	0.1897	<u>0.1810</u>	0.9206	0.9164	0.9075	0.9006
Proposed	0.2144	0.2009	0.1865	0.1801	0.9238	0.9201	0.9134	0.9074

(0.1% noise) task, the Frobenius norm of A is 2051.5, k_y is set to 0.01, k_e is set to 0, and $T^T T$ is set to -0.5Δ , where Δ denotes a 2 dimensional discrete Laplacian operator.

4 Results

We conducted a comparative analysis between I²SB, CDDB, CDDB deep, and our proposed MESB. Additionally, we included another comparison method degenerated from MESB by setting k_y to positive infinity, and k_e and T to 0. We term this method "Project" since, in each reverse step, it projects \hat{X}_0 onto the plane $AX = y$. The number of CG iterations for Project in each reverse step is set to 5. For a fair comparison, all tested methods use the same trained models, and the hyperparameters during testing are optimized to the best of our ability. The hyperparameter settings for CDDB and CDDB deep are detailed in Appendix A.2.2. Representative results for natural images are visualized in Figure 1, and medical images in Figure 2. For quantitative analysis, we calculated learned perceptual image patch similarities (LPIPS)[20] to evaluate the texture restoration ability of the tested methods and structural similarity index measures (SSIMs) to assess the fidelity of the tested methods to the ground truth. These quantitative results are detailed in Tables 1, 2, and 3. See Appendix A.3 for additional results, including ablation studies and statistical significance tests.

In the deblur-gauss (no noise) task, our proposed MESB consistently outperformed all other methods across all generative steps N . MESB significantly outperforms I²SB, CDDB, and CDDB deep, with improvements of 20% to 30% in LPIPS and increases of 0.015 to 0.025 in SSIMs. This is further supported by the visualization results in Figure 1, where MESB shows superior restoration details in areas like cherries, pant pleats, and fishing nets. Compared to the second-place method, Project, our proposed MESB achieved about a 3% improvement in LPIPS and a 0.003 increase in SSIMs.

In the sr4x-bicubic (1% noise) task, when N equals to 10, our proposed MESB achieves the best results in terms of both LPIPS and SSIMs. As visualized in Figure 1, MESB demonstrates superior restoration details in areas like pig’s knuckles, dog’s eyes, and cup mouths. Since the system matrix in this task nearly satisfies the conditions described in Theorem 2, the performance difference between MESB and CDDB decreases as the generative steps N increase. For N equals to 50 and 100, CDDB deep achieves the best results, but the computation of the U-net Jacobian makes it approximately three times more computationally expensive than other methods (see Appendix A.2.1 for computation time). Project does not perform well in this task due to its sensitivity to noise. As highlighted by the yellow arrows in Figure 1, Project introduces unrealistic artifacts. Compared to Project, MESB achieves a 5% to 10% improvement in LPIPS and a 0.005 to 0.01 increase in SSIMs.

In the CT sparse view reconstruction (0.1% noise) task, our proposed MESB consistently outperformed all other methods across all generative steps N . Compared with CDDB and CDDB deep, MESB achieved a 0.5% to 4% improvement in LPIPS and a 0.003 to 0.007 increase in SSIMs. As shown in Figure 2, MESB demonstrates superior detail restoration in mammary glands and corrects the inaccurately generated pulmonary vein seen in I²SB. Project achieved second place in terms of SSIM, but its LPIPS were worse than those of I²SB due to overfitting to noise in the measurement. Compared with Project, MESB achieved a 2% to 7% improvement in LPIPS and a 0.003 increase in SSIMs.

Overall, while the performances of CDDB and CDDB deep are significantly influenced by the system matrix, and Project is sensitive to noise in measurements, our proposed MESB consistently achieves good performance across all three tasks.

5 Conclusion and Discussion

In conclusion, we propose MESB, a novel model that establishes Schrödinger Bridges between the distribution of corrupted images and the distribution of clean images given measurements. Based on optimal transport theory, we embed measurements into the marginal condition of the Schrödinger Bridge, deriving both the forward and backward processes. We also provide an explanation of MESB and its connections with CDDB and CDDB deep. Our proposed MESB demonstrates robustness to noise and outperforms existing Schrödinger Bridge-based inverse problem solvers in both natural and medical image tasks.

MESB shows promise for further refinement in the design of the transformation matrix T . Currently, T is set to 0 for natural images and as a gradient operator for CT images. A more dedicated design of T may incorporate additional prior knowledge and further enhance the performance of MESB. Additionally, while measurements are not necessary during training, paired clean and corrupted images are required. In future work, we will explore extending MESB to unpaired data and broadening the application scenarios for MESB.

References

- [1] Y. Song and S. Ermon, “Generative modeling by estimating gradients of the data distribution,” *Advances in neural information processing systems*, vol. 32, 2019.
- [2] J. Ho, A. Jain, and P. Abbeel, “Denoising diffusion probabilistic models,” *Advances in neural information processing systems*, vol. 33, pp. 6840–6851, 2020.
- [3] Y. Song, J. Sohl-Dickstein, D. P. Kingma, A. Kumar, S. Ermon, and B. Poole, “Score-based generative modeling through stochastic differential equations,” *arXiv preprint arXiv:2011.13456*, 2020.
- [4] H. Chung, S. Lee, and J. C. Ye, “Fast diffusion sampler for inverse problems by geometric decomposition,” *arXiv preprint arXiv:2303.05754*, 2023.
- [5] H. Chung, J. Kim, M. T. Mccann, M. L. Klasky, and J. C. Ye, “Diffusion posterior sampling for general noisy inverse problems,” *arXiv preprint arXiv:2209.14687*, 2022.
- [6] H. Chung, B. Sim, D. Ryu, and J. C. Ye, “Improving diffusion models for inverse problems using manifold constraints,” *Advances in Neural Information Processing Systems*, vol. 35, pp. 25 683–25 696, 2022.
- [7] B. Song, S. M. Kwon, Z. Zhang, X. Hu, Q. Qu, and L. Shen, “Solving inverse problems with latent diffusion models via hard data consistency,” *arXiv preprint arXiv:2307.08123*, 2023.
- [8] B. Kim, G. Kwon, K. Kim, and J. C. Ye, “Unpaired image-to-image translation via neural schrödinger bridge,” *arXiv preprint arXiv:2305.15086*, 2023.
- [9] M. Delbracio and P. Milanfar, “Inversion by direct iteration: An alternative to denoising diffusion for image restoration,” *arXiv preprint arXiv:2303.11435*, 2023.
- [10] T. Chen, G.-H. Liu, and E. A. Theodorou, “Likelihood training of schrödinger bridge using forward-backward sdes theory,” *arXiv preprint arXiv:2110.11291*, 2021.
- [11] Y. Chen, T. T. Georgiou, and M. Pavon, “Stochastic control liaisons: Richard sinkhorn meets gaspard monge on a schrodinger bridge,” *Siam Review*, vol. 63, no. 2, pp. 249–313, 2021.
- [12] V. De Bortoli, J. Thornton, J. Heng, and A. Doucet, “Diffusion schrödinger bridge with applications to score-based generative modeling,” *Advances in Neural Information Processing Systems*, vol. 34, pp. 17 695–17 709, 2021.
- [13] G.-H. Liu, A. Vahdat, D.-A. Huang, E. A. Theodorou, W. Nie, and A. Anandkumar, “T²sb: Image-to-image schrödinger bridge,” *arXiv preprint arXiv:2302.05872*, 2023.
- [14] H. Chung, J. Kim, and J. C. Ye, “Direct diffusion bridge using data consistency for inverse problems,” *Advances in Neural Information Processing Systems*, vol. 36, 2024.

- [15] C. Léonard, “A survey of the schrödinger odinger problem and some of its connections with optimal transport,” *arXiv preprint arXiv:1308.0215*, 2013.
- [16] P. Vincent, “A connection between score matching and denoising autoencoders,” *Neural computation*, vol. 23, no. 7, pp. 1661–1674, 2011.
- [17] S. R. Garcia, M. O. Patterson, and W. T. Ross, “Partially isometric matrices: a brief and selective survey,” *arXiv preprint arXiv:1903.11648*, 2019.
- [18] J. Deng, W. Dong, R. Socher, L.-J. Li, K. Li, and L. Fei-Fei, “Imagenet: A large-scale hierarchical image database,” in *2009 IEEE conference on computer vision and pattern recognition*. Ieee, 2009, pp. 248–255.
- [19] P. Yu, H. Zhang, H. Kang, W. Tang, C. W. Arnold, and R. Zhang, “Rplhr-ct dataset and transformer baseline for volumetric super-resolution from ct scans,” in *International Conference on Medical Image Computing and Computer-Assisted Intervention*. Springer, 2022, pp. 344–353.
- [20] R. Zhang, P. Isola, A. A. Efros, E. Shechtman, and O. Wang, “The unreasonable effectiveness of deep features as a perceptual metric,” in *Proceedings of the IEEE conference on computer vision and pattern recognition*, 2018, pp. 586–595.

A Appendix

A.1 Proof

A.1.1 Proof of Theorem 1

To prove Theorem 1, we first verify that the Ψ expressed in equation (12) satisfies:

$$\frac{\partial \Psi}{\partial t} = -\frac{1}{2}\beta\Delta\Psi. \quad (32)$$

This is because:

$$\begin{aligned} \frac{\partial \Psi}{\partial t} &= \frac{\partial \Psi}{\partial \sigma_t^2} \frac{\partial \sigma_t^2}{\partial t}, \\ &= -\frac{1}{2}\beta\Psi \left(\frac{(X_t - X_{corrupt})^\top (X_t - X_{corrupt})}{\sigma_t^4} - \frac{d}{\sigma_t^2} \right), \\ &= -\frac{1}{2}\beta\Delta\Psi. \end{aligned} \quad (33)$$

In a similar way, $\hat{\Psi}_{X_0}(X_t, t)$ satisfies:

$$\frac{\partial \hat{\Psi}_{X_0}}{\partial t} = \frac{1}{2}\beta\Delta\hat{\Psi}_{X_0}. \quad (34)$$

Hence, the $\hat{\Psi}$ expressed in equation (13) satisfies:

$$\begin{aligned} \frac{\partial \hat{\Psi}}{\partial t} &= \int \frac{\partial \hat{\Psi}_{X_0}}{\partial t} q_{clean}(X_0|X_{corrupt}, y) dX_0, \\ &= \frac{1}{2}\beta\Delta\hat{\Psi}. \end{aligned} \quad (35)$$

Therefore, Ψ and $\hat{\Psi}$ satisfy the PDEs (3). For the margin conditions (4),

$$\Psi(X_0, 0) = \frac{1}{C_{X_0}}, \quad (36)$$

where C_{X_0} is expressed in equation (15), and

$$\begin{aligned} \hat{\Psi}(X_0, 0) &= \int C_X \delta(X_0 - X) q_{clean}(X|X_{corrupt}, y) dX, \\ &= C_{X_0} q_{clean}(X_0|X_{corrupt}, y), \end{aligned} \quad (37)$$

Table 4: The sampling time of tested methods on different tasks.

sec./(iter · batch size)	I ² SB	Project	CDDB	CDDB deep	Proposed
Deblur-gauss	0.031	0.032	0.031	0.096	0.032
Sr4x-bicubic	0.031	0.032	0.031	0.096	0.032
CT sparse view	0.043	0.060	0.050	0.184	0.060

then

$$\Psi(X_0, 0) \hat{\Psi}(X_0, 0) = p_A, \quad (38)$$

where p_A is defined as equation (10). Also

$$\Psi(X_1, 1) = \delta(X_1 - X_{corrupt}), \quad (39)$$

and because $\hat{\Psi}_{X_0}(X_1 = X_{corrupt}, 1)$ equals to 1, we have:

$$\begin{aligned} \Psi(X_1, 1) \hat{\Psi}(X_1, 1) &= \delta(X_1 - X_{corrupt}) \int \hat{\Psi}_{X_0}(X_1, 1) q_{clean}(X_0|X_{corrupt}, y) dX_0, \\ &= \delta(X_1 - X_{corrupt}), \\ &= p_B. \end{aligned} \quad (40)$$

That completes the proof.

A.1.2 Proof of equation (18)

This equation can be proved by substituting equation (17) into equation (13), calculating the integration regarding to X_0 and finally calculating the log gradient regarding to X_t .

A.1.3 Proof of Theorem 2

According to the definition of the partially isometric matrix, we have:

$$A = \alpha_0 A A^\top A. \quad (41)$$

Also because A is row full rank, for any y , there always exists an X_0 such that $y = AX_0$. We use $f(X)$ to represent:

$$f(X) = \|X - \hat{X}_0\|_2^2 + k\|A(X - X_0)\|_2^2, \quad (42)$$

then

$$\frac{df}{dX} = 2 \left((X - \hat{X}_0) + kA^\top A(X - X_0) \right). \quad (43)$$

According to equation (27), we have

$$\hat{X}_{0,new}^{CDDB} = \hat{X}_0 + \alpha A^\top A (X_0 - \hat{X}_0). \quad (44)$$

Using equation 41 and substituting X in equation (43) with $\hat{X}_{0,new}^{CDDB}$, we figure out that if $\alpha = \frac{\alpha_0 k}{\alpha_0 + k}$, $\frac{df}{dX}$ equals to 0 when X equals to $\hat{X}_{0,new}^{CDDB}$. Therefore, $\hat{X}_{0,new}^{CDDB}$ is the optimal point for minimizing $f(X)$. That completes the proof.

A.1.4 Proof of Theorem 3

To prove theorem 3, we have

$$\nabla \log \hat{\Psi} = \nabla \log (\hat{\Psi} \Psi) - \nabla \log \Psi. \quad (45)$$

Noting that

$$q(X_t|X_0, X_{corrupt}) = k_{X_t} \Psi \hat{\Psi}_{X_0}, \quad (46)$$

where q is defined in equation (5), X_1 is substituted by $X_{corrupt}$, and k_{X_t} denotes a constant independent of X_0 , we have:

$$\nabla \log \hat{\Psi} = \nabla \log \left(\frac{1}{k_{X_t}} \int q(X_t|X_0, X_{corrupt}) q_{clean}(X_0|X_{corrupt}, y) dX_0 \right) - \nabla \log \Psi. \quad (47)$$

Table 5: Ablation study for k_y in the CT sparse view reconstruction (0.1% noise) task. **Bold**: Best.

$k_y \setminus N$	LPIPS				SSIM			
	10	20	50	100	10	20	50	100
0.0025	0.2213	0.2063	0.1902	0.1836	0.9143	0.9096	0.9014	0.8947
0.005	0.2176	0.2037	0.1889	0.1826	0.9151	0.9108	0.9029	0.8965
0.01	0.2157	0.2028	0.1892	0.1832	0.9154	0.9112	0.9037	0.8973
0.025	0.2165	0.2042	0.1916	0.1863	0.9147	0.9107	0.9034	0.8971
0.05	0.2180	0.2061	0.1941	0.1892	0.9139	0.9100	0.9027	0.8963

Given X_0 and $X_{corrupt}$, X_t is independent of y , therefore

$$\begin{aligned}
 \nabla \log \hat{\Psi} &= -\nabla \log k_{X_t} + \nabla \log q(X_t | X_{corrupt}, y) - \nabla \log \Psi, \\
 &= -\nabla \log k_{X_t} + \nabla \log q(X_t | X_{corrupt}) - \nabla \log \Psi + \nabla \log q(y | X_t, X_{corrupt}), \\
 &= \nabla \log \left(\int \hat{\Psi}_{X_0} q_{clean}(X_0 | X_{corrupt}) dX_0 \right) + \nabla \log q(y | X_t, X_{corrupt}).
 \end{aligned} \tag{48}$$

The first term independent of measurement y is learned by score matching and the second term is computed using the assumption (30). Therefore,

$$\nabla \log \hat{\Psi} = -\frac{1}{\sigma_t^2} (X_t - \hat{X}_0(X_t)) - \frac{1}{2\sigma^2} \nabla_{X_t} \|A\hat{X}_0(X_t) - y\|_2^2, \tag{49}$$

where the expected mean \hat{X}_0 is defined as:

$$\hat{X}_0 = \int X_0 q(X_0 | X_t, X_{corrupt}) dX_0. \tag{50}$$

That completes the proof.

A.2 Experimental Details

A.2.1 Running Statistics

All experiments were run using a single A100-SXM4-40GB GPU. The sampling time of tested methods on different tasks is detailed in Table 4.

A.2.2 Hyperparameters for Comparison Methods

In the deblur-gauss (no noise) task, the step length α is set to 10 for CDDb and 0.01 for CDDb deep. In the sr4x-bicubic (1% noise) task, α is set to 10 for CDDb and 4 for CDDb deep. For the CT sparse view reconstruction (0.1% noise) task, α is set to 0.001 for CDDb and $\frac{0.05}{\|A\hat{X}_0 - y\|_2}$ for CDDb deep.

A.3 Additional Results

A.3.1 Ablation Studies

We conducted ablation studies on the hyperparameters k_y and k_e of our proposed MESB. First, we examined the impact of k_y in CT sparse view reconstruction (0.1% noise) task. We randomly selected 32 slices from the test dataset, fixing k_e to 0 and T to -0.5Δ . We varied k_y from 0.0025 to 0.05, with quantitative results detailed in Table 5. As k_y increases, LPIPS and SSIMs initially become better and then go worse for all generative steps N , indicating that an optimal k_y enhances the performance of MESB.

Next, we studied the impact of k_e in deblur-gauss (no noise) task. We randomly selected 180 natural images from the validation dataset of Imagenet 256x256, and fixed k_y to positive infinity and T to 0.

We set k_e to $k_E \frac{\sigma_n^2 \bar{\sigma}_n^2}{\sigma_A^4 \bar{\sigma}_N^2}$, with k_E ranging from 0 to 100, and quantitative results detailed in Table 6. As k_E increases, LPIPS and SSIMs initially become better and then go worse for all generative steps N , indicating that an optimal k_E enhances the performance of MESB.

Table 6: Ablation study for k_E in the deblur gauss (no noise) task. **Bold**: Best.

$k_E \setminus N$	LPIPS				SSIM			
	10	20	50	100	10	20	50	100
0	0.0451	0.0434	0.0421	0.0413	0.9701	0.9713	0.9724	0.9732
10	0.0433	0.0409	0.0393	0.0386	0.9725	0.9741	0.9753	0.9758
20	0.0435	0.0410	0.0394	0.0388	0.9727	0.9746	0.9757	0.9760
50	0.0443	0.0423	0.0406	0.0399	0.9729	0.9744	0.9755	0.9760
100	0.0455	0.0437	0.0423	0.0417	0.9727	0.9741	0.9751	0.9755

A.3.2 Statistical Significance Tests

We performed dependent t-tests to compare the LPIPS and SSIMs of our proposed MESB with those of the comparison methods across different images. The p-values were all less than 0.04, indicating that the differences in mean values shown in Tables 1, 2, and 3 are statistically significant.